

Research Article

Migration and Residual Trapping of Immiscible Fluids during Cyclic Injection: Pore-Scale Observation and Quantitative Analysis

Haejin Ahn,¹ Seon-Ok Kim,² Minhee Lee,³ and Sookyun Wang² 

¹GeoGreen21 Co. Ltd., Seoul 08376, Republic of Korea

²Department of Energy Resources Engineering, Pukyong National University, Busan 48513, Republic of Korea

³Department of Earth Environmental Sciences, Pukyong National University, Busan 48513, Republic of Korea

Correspondence should be addressed to Sookyun Wang; sookyun@pknu.ac.kr

Received 18 October 2019; Accepted 6 January 2020; Published 16 July 2020

Academic Editor: Fabien Magri

Copyright © 2020 Haejin Ahn et al. This is an open access article distributed under the Creative Commons Attribution License, which permits unrestricted use, distribution, and reproduction in any medium, provided the original work is properly cited.

Geological CO₂ sequestration (GCS) is one of the most promising technologies for mitigating greenhouse gas emission into the atmosphere. In GCS operations, residual trapping is the most favorable form of a trapping mechanism because of its storage security and capacity. In this study, the effects of cyclic injection of CO₂-water on the immiscible displacement and residual trapping in pore networks were examined. For the purpose, a series of injection experiments with five sets of drainage-imbibition cycles were performed using 2D transparent micromodels and a pair of proxy fluids, *n*-hexane, and deionized water. The multiphase flow and immiscible displacement phenomena during drainage and imbibition processes in pore networks were visually observed, and the temporal and spatial changes in distribution and saturation of the two immiscible fluids were quantitatively estimated at the pore scale using image analysis techniques. The results showed that the mobile region of invading fluids decreased asymptotically as the randomly diverged flow paths gradually converged into less ramified ones over multiple cycles. Such decrease was accompanied by a gradual increase of the immobile region, which consists of tiny blobs and clusters of immiscible fluids. The immobile region expanded as streams previously formed by the insertion of one fluid dispersed into numerous isolated, small-scale blobs as the other fluid was newly injected. These processes repeated until the immobile region approached the main flow channels. The observations and analyses in this study implied that the application of cyclic injection in GCS operations may be used to store large-scale CO₂ volume in small-scale dispersed forms, which may significantly improve the effectiveness and security of geological CO₂ sequestration.

1. Introduction

Geological CO₂ sequestration (GCS) is one of the most promising technologies for mitigating greenhouse gas emission into the atmosphere. It involves collecting CO₂ from various point sources such as power plants, refineries, and industrial plants at a large scale and storing it in deep geological formations such as depleted oil/gas fields, coal beds, or saline aquifers [1–3]. Once CO₂ is injected into porous strata, it can be securely stored for a geological time scale through various trapping mechanisms, which include structural trapping due to blockage by impermeable caprocks for an upward buoyant CO₂ plume, residual trapping by isolating CO₂ in

pore spaces by capillary forces or surrounding immiscible bubbles, solubility trapping due to dissolution of free-phase CO₂ into porewater, and mineral trapping due to geochemical binding of dissolved carbonate species to rock formations [2, 4, 5]. Although structural trapping is immediate and the most dominant mechanism, its security mainly relies on the structural integrity of caprocks [6, 7]. Solubility and mineral trapping are semipermanent forms of trapping mechanisms, but they involve relatively or extremely slow reactions that depend on the chemistry of rock and porewater [8, 9]. Compared to them, residual trapping is the most favorable form of a trapping mechanism because of its storage security and capacity. In the processes of residual trapping, CO₂ as

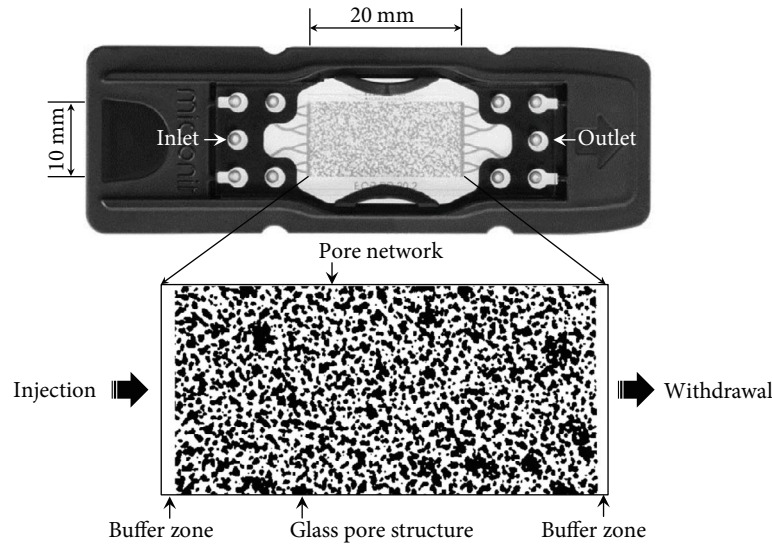


FIGURE 1: Physical network micromodel and its pore structure.

continuous plumes is broken up and dispersed as innumerable tiny CO_2 blobs and ganglia. Reduced buoyancy acting on small-scale CO_2 decreases the potential risk of upward migration and leakage, and its high specific surface area facilitates dissolution of CO_2 into the surrounding porewater and expedites the progress to more secure forms of trapping: dissolution and mineral trappings [10, 11]. In addition, the contribution of residual trapping to overall CO_2 storage capacity is reportedly greater than that of both dissolution and mineral trappings for a relatively long time [12, 13]. In order to improve effectiveness and security in GCS operations, therefore, appropriate strategies for maximizing residual trapping should be developed and applied [14].

Of various injection strategies for GCS, cyclic CO_2 -brine injection has drawn significant interest from researchers in the related area for improving residual trapping by alternatively injecting CO_2 with water [14–22]. Despite technical difficulties in extracting and discharging a significant amount of brine from deep targeting reservoirs, the use of cyclic CO_2 -brine injection has been proposed as an effective strategy for mitigating possible risks of leakage by dispersing CO_2 as continuous streams into innumerable tiny blobs and inducing residual trapping which can limit upward mobility and facilitate dissolution of free-phase CO_2 [9, 22]. For investigating the effects of cyclic or sequential injection of CO_2 with brine for GCS operations, Saeedi et al. [15] conducted core-flooding experiments for sandstone samples with different permeabilities and porosities through nuclear magnetic resonance during seven injection cycles. Kimbrel et al. [18] investigated effects of fluid parameters, such as interfacial tension, viscosities, and flow rate, on capillary trapping during a set of drainage-imbibition cycles. Herring et al. [19] used X-ray tomographic imaging for sandstone cores to demonstrate the effectiveness and hysteretic dependency of cyclic injection in improving residual trapping. Malekzadeh et al. [20] developed an analytical solution for a mathematical model describing saturation distribution in a drainage-imbibition process. Edlmann et al. [22] presented the results of six cycles

of CO_2 -brine injection on injectivity through observations and modeling. In addition, many researchers and engineers in the area of petroleum engineering also conducted experiments and mathematical modeling on use of cyclic injection of CO_2 for increasing capillary trapping and recovery efficiency in EOR operations [23–28].

In this study, we carried out a series of cyclic injection experiments of immiscible fluids with five drainage-imbibition cycles using 2D transparent micromodels and two proxy fluids, *n*-hexane and deionized water, for simulating CO_2 and porewater in GCS operations. Immiscible displacement phenomena during drainage and imbibition processes in pore networks in micromodels were visually observed, and distribution and saturation of hexane and water were quantitatively estimated using image analysis techniques. Through observation and analysis, the effects of cyclic injection on the migration and distribution of invading and residing fluids have been investigated. Results from this study may provide detailed understanding of the immiscible displacement and residual trapping of CO_2 in aquifers resulting from cyclic injection of CO_2 and water in GCS.

2. Materials and Methods

2.1. Micromodels. Highly transparent micromodels fabricated of borosilicate glass (Micronit Microfluidics BV) were used in experiments. Symmetrically etched on silica plates, the two-dimensional pore structure (a patterned area of 20×10 mm) in the micromodel is designed to effectively represent the migration and distribution of invading and residing fluids and their immiscible displacement processes in porous media (Figure 1). Pore depth and pore volume excluding buffer zones inside the micromodel were $20 \mu\text{m}$ and $2.3 \mu\text{L}$, respectively. Porosity and permeability were measured as 0.57 and $2.47 \times 10^{-12} \text{ m}^2$, respectively. The contact angle of water in the micromodel was measured as $20^\circ \sim 24^\circ$, and the wettability of its inner surface was defined as water wet. As seen in Figure 1, there were eight

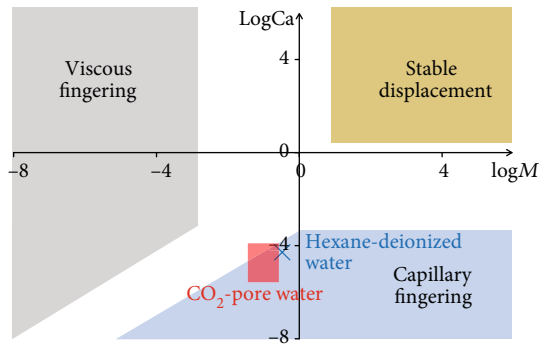


FIGURE 2: $\log M$ - $\log Ca$ phase diagram showing three immiscible displacement patterns of fluids in porous media and the area of the $scCO_2$ -water and hexane-water displacement experiments (adapted from Lenormand et al. [32]).

inflowing channels into the pore network in the micromodels and the flow rates of the channels were not controllable and could not be identical. Inflowing sequence and rate might, therefore, affect the randomness in the migration and distribution patterns of invading and residing fluids.

2.2. Proxy Fluids for Supercritical CO_2 and Brine. Based on experimental measurements of viscosity, density, and interfacial tension of supercritical CO_2 , $nM = \mu_2/\mu_1$ and brine at reservoir conditions reported in previous research [10, 29–31], *n*-hexane (“hexane” in the latter) and deionized water (“water” hereafter) were selected as proxy fluids. Viscosity ratio (n , where μ_1 and μ_2 are the viscosity of residing and invading fluids, respectively) and capillary number, which is defined as the ratio of viscous force to capillary force ($Ca = \mu_2 v_2 / \gamma \cos \theta$, where v_2 , γ , and θ are the velocity of invading fluid, interfacial tension between invading and residing fluids, and contact angle, respectively), of the pairs under ambient conditions have values ($\log M = -0.48$; $\log Ca = -4.29$) similar to those of supercritical CO_2 and brine at geological CO_2 sequestration conditions ($\log M = -1.29 \sim -0.76$; $\log Ca = -5.33 \sim -4.55$) to approximate flow processes on a pore scale [18, 19]. Figure 2 compares the capillary numbers and viscosity ratios for hexane and water at ambient conditions to those of supercritical CO_2 and brine under geological CO_2 sequestration conditions in the $\log M$ - $\log Ca$ plot classifying invading patterns presented by Lenormand et al. [32]. The experimental conditions using proxy fluids in this study were within the transition region between regions for viscous fingering and capillary fingering in Figure 2. Although the pair of proxy fluids could not provide direct representation of supercritical CO_2 and brine, both combinations might show similar patterns in dynamic behaviors of multiphase flow processes in pore networks and could provide fundamental understanding of geological CO_2 sequestration operations. Viscosity and density data of hexane and water were referenced from the literature (Table 1) [33, 34]. In order to differentiate the immiscible colorless fluids in pore networks for image analysis as well as visual observation, methylene blue ($C_{16}H_{18}ClN_3S \cdot 2 \sim 3H_2O$, Junsei) and Sudan

IV ($C_{24}H_{20}N_{40}O$, Sigma-Aldrich) were used to dye water and hexane in blue and red, respectively.

2.3. Experimental Setups. The experimental setup for pore-scale observation on immiscible displacement processes in artificial pore networks is shown in Figure 3. The micromodel was kept in place by a chip holder and was horizontally placed to minimize the effect of gravity on flow. For cyclic injection of the two fluids, two high-precision syringe pumps (NE-300, New Era Pump Systems Inc.) equipped with 10 mL syringes (Luer-Lock-type plastic syringe, Top Syringe Manufacturing Company Pvt. Ltd.) were connected to the inlet of the micromodel through a Y-type connector (1/8" ID PVC tubing, New Era Pump System Inc.) and 1/16" Teflon™ tubes. The withdrawal system consisted of a high-precision syringe pump equipped with a 10 mL syringe connected to the outlet of the micromodel. Simultaneous injection and withdrawal at a constant flow rate were used to avoid compression build-up and to maintain the fluid flow throughout the entire system as steady and stable. The discharged fluids were guided through a 1/16" Teflon™ tube out of the micromodel and collected in the syringe for withdrawal. To visualize the dynamic processes taking place in the micromodel, a high-resolution microscope camera (DA-Ri1-U3, Nikon) was positioned above the viewing area of the micromodel for allowing close observation and image transfer to a PC with image processing software (NIS-Elements D, Nikon). Below the micromodel, a LED light source was placed with light diffuser papers to provide light at a constant intensity.

2.4. Experimental Procedure. A series of cyclic injection experiments were carried out to investigate the effects of periodic drainage-imbibition processes on the flow and displacement of immiscible fluids in a microscale pore network. Prior to each experiment, the micromodel and connecting tubes were saturated with water using a high-pressure pump (260D Syringe Pump, Teledyne Isco) at an extremely slow flow rate of 1 mL/hr to ensure that no air was captured in the pore network. Two injection syringes filled with hexane and water were installed in two injection pumps, and an empty syringe was installed in one withdrawal pump and was connected with the micromodel through tubes and connectors, as depicted in Figure 3. A single set of injection experiments consisted of a total of five drainage-imbibition cycles. The first drainage cycle was initiated by injecting the nonwetting fluid, hexane, in the water-saturated micromodel and, simultaneously, by withdrawing the wetting fluid, water, at equal, reverse flow rate from the micromodel. After the drainage cycle, the first imbibition cycle followed by injecting water as a wetting and chase fluid. For each drainage or imbibition cycle, 4.35 pore volumes of hexane or water was injected at a constant flow rate of $2 \mu L/min$ for 5 minutes and a 10-minute break followed for stabilizing the flow and distribution of fluids in the pore network. This procedure consisted of the first drainage-imbibition cycle and was repeated four more times. Throughout the entire injection experiment, microscopic images were captured and recorded sequentially for further quantitative analysis.

TABLE 1: Fluid properties and interfacial tension of hexane and water at ambient pressure.

Temperature (°C)	<i>n</i> -Hexane		Deionized water		IFT (mN/m)
	Density (kg/m ³)	Viscosity (cP)	Density (kg/m ³)	Viscosity (cP)	
25	654.80	0.297	997.05	0.890	50.38

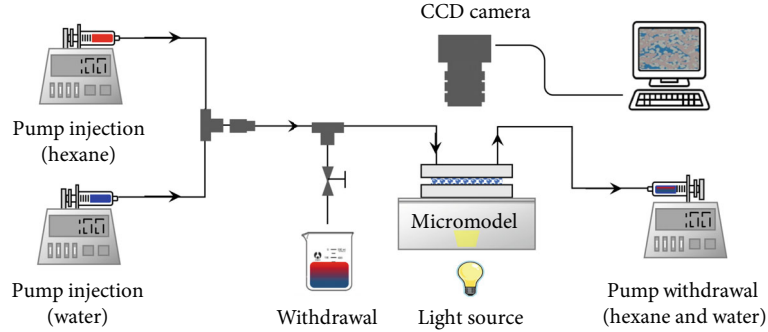


FIGURE 3: Schematic diagram of the experimental setup for cyclic injection of immiscible fluids.

After the completion of each experiment, the micromodel was removed from the holder, flushed with methanol (CH_3OH , Duksan), acetone (CH_3COCH_3 , Junsei), and water using a high-pressure pump to remove all the remnants, such as hexane and dyes, which might affect surface properties of the pore network, and was oven-dried at 50°C for 24 hours. This cleaning procedure was repeated prior to every experiment to ensure that the initial conditions of micromodels were identical for each application.

2.5. Image Processing and Analysis. The procedure taken was as follows:

- (1) The multiphase flow and displacement behavior in the micromodels were visually observed and recorded as an AVI format with a resolution of $1280 \text{ pixel} \times 1024 \text{ pixel}$
- (2) Using an image-processing software, ImageJ (US National Institutes of Health), we transformed the video images to image files for quantitative image analysis. Raw images extracted from video were RGB images composed of color pixels with red, green, and blue values ranging from 0 (darkest) to 255 (brightest), with a time interval of 0.22 seconds. Figures 4(a) and 4(b) display a part of the pore network in the micromodel in which the pore space was fully saturated with water prior to hexane injection and partially occupied by water and hexane after the following imbibition or drainage cycles, respectively
- (3) In order to determine a threshold value for creating binary images, we converted RGB images to gray images with brightness ranging from 0 to 255 using ImageJ (Figure 4(c)). The contrast ratio in the binary images was increased to enhance sharpness and to facilitate the distinction among fluids and pore structure. Noise due to the change in contrast ratio was reduced by blurring

- (4) Grey images were then converted into black-and-white binary image using an in-house MATLAB program. Based on a certain threshold specified, each grey pixel was converted either into a white pixel, representing the area occupied by porewater, or into a black pixel, representing the area occupied by hexane or glass (Figure 4(d))
- (5) To differentiate hexane and glass, pixel values of Figure 4(d) were compared to those of the initial binary images, in which pore spaces were saturated with water (converted from Figure 4(a), not shown), and new binary images were created, in which glass and residual water were represented as black pixels, whereas pore spaces filled with hexane were represented as white pixels (Figure 4(e))
- (6) Then, we created multicolor images (Figure 4(f)) by coloring water in Figure 4(d) in blue and hexane in Figure 4(e) in red and by superposing them on the binary image of a clean micromodel. The multicolor images allowed investigation of the changes in spatio-temporal distribution of wetting and nonwetting fluids by creating distinctive boundaries between phases, and thus enabling quantitative analysis of fluid saturations. After the completion of imbibition or drainage processes, the saturation of water or hexane was calculated as the ratio of number of pixels of a region occupied by a corresponding fluid to those of total pore space
- (7) Finally, the last step of image processing was to analyze fluid mobility, in which the fluids in the pore network were classified as mobile or immobile fractions according to their connectivity. Mobile fractions are identified as continuous streams of an invading fluid connecting from inlets to outlets, which are flowing, whereas immobile fractions are separated blobs or clusters of fluids that are isolated from the streams or trapped in pore spaces, which are stagnant [35]

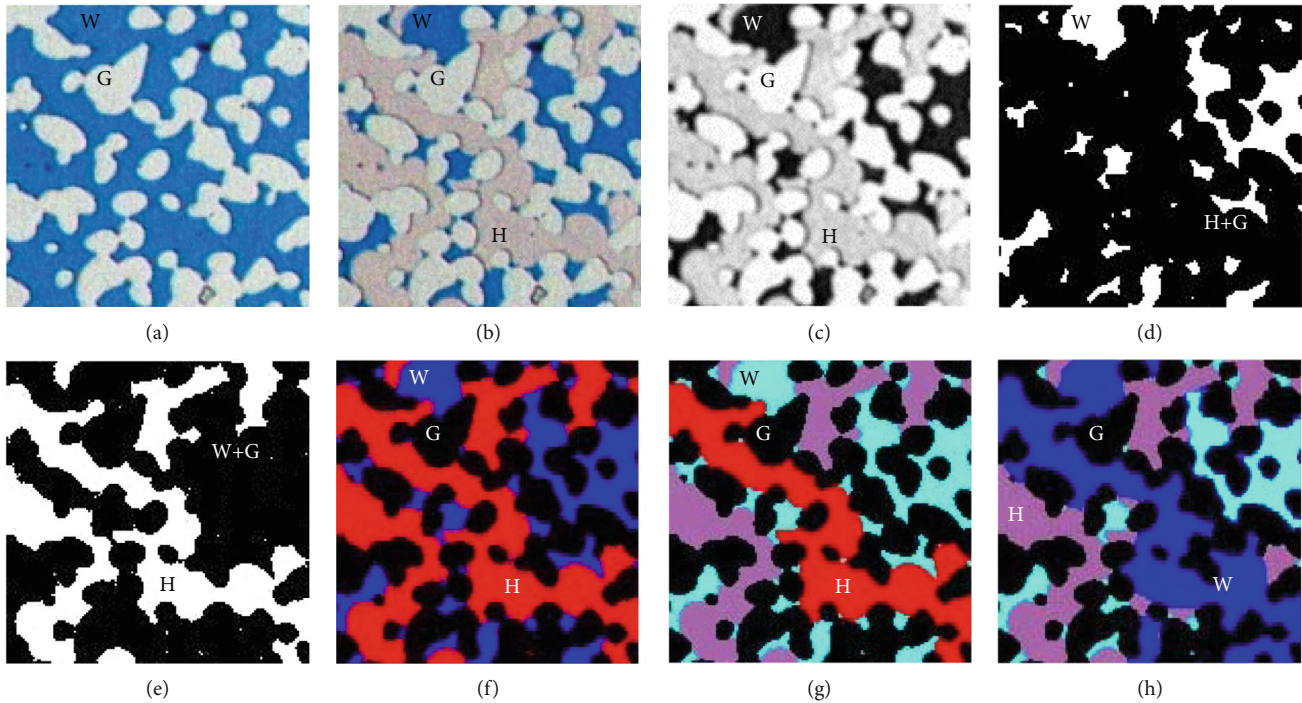


FIGURE 4: Image processing procedure (W: water; H: hexane; G: glass): (a) a raw image (initially saturated with water), (b) a raw image (saturated with water and hexane), (c) the grey image of (b), (d) the binary image of (c) (after applying threshold, W and H+G), (e) the binary image from (d) subtracting the binary image of (a) (H and W+G), (f) the multicolored image from (d) and (e) (hexane in red and water in blue), (g) the multicolored image from (f) in a drainage cycle (immobile hexane in purple and immobile water in cyan), and (h) the multicolored image from (f) in an imbibition cycle.

(8) In multicolored images after drainage processes (Figure 4(f)), immobile fractions of hexane were selected and colored in purple, while all the water in the residual and immobile phases was colored in cyan, as in Figure 4(g). In the same way, all the hexane, which was in the residual phase, and immobile fractions of water were colored in purple and cyan, respectively, in the multicolored images after imbibition processes (Figure 4(h)). The final multicolored images (Figures 4(g) and 4(h)) allowed us to understand the temporal and spatial distribution of immiscible fluids in the pore networks and to conduct quantitative analysis on their mobility and resulting dynamic behaviors

3. Results and Discussions

In this experiment, hexane and water were injected cyclically into a horizontal micromodel, which was initially fully saturated with water. Figure 5 shows the sequential distributions of two immiscible fluids, hexane and water, in the micromodel after the completion of every drainage and imbibition cycles of the representative case. Depending on its connectivity, each fluid is classified as mobile or immobile fractions with different colors in the figure. The red and purple areas represent mobile and immobile fractions of hexane, respectively, and the blue and cyan areas represent those of water, respectively. The black area is the matrix. Mobile or immo-

bile regions refer to multiple pore spaces occupied by mobile or immobile fractions of two immiscible fluids, respectively.

As can be observed in Figure 5, hexane (colored in red and purple) occupied more pore space than did water (colored in blue and cyan) at steady state after drainage cycles in which hexane was injected and so did water after imbibition cycles. That is, while passing through pore networks in a micromodel, the invading fluid displaced residing fluids and took up pore spaces. Comparing images of drainage cycles D1~D5, one can see that the mobile fraction of hexane, colored in red, visibly decreased as cyclic injection continued, whereas the immobile fractions of hexane, colored in purple, increased. The same trends applied to mobile and immobile fractions of water, colored in blue and cyan, respectively, in imbibition cycles I1~I5. That is, the flow of an invading fluid converged on fewer active flow paths for both hexane and water and the converged flow paths of hexane and water at later cycles were getting remarkably overlapped over cycles. Though not clearly visible, the connectivity of blobs and clusters of immobile fractions seemed to be decreasing for both fluids in the figure. These brief observations were confirmed by further quantitative analysis.

The evolution of hexane saturation over five drainage-imbibition cycles is displayed in Figure 6. As can be clearly seen, hexane saturation increased in drainage cycles and decreased in imbibition cycles. General patterns of saturation change in each cycle in the figure consisted of a substantial increase (in drainage cycles) or decrease (in imbibition cycles) and a flattening out after a breakthrough of invading

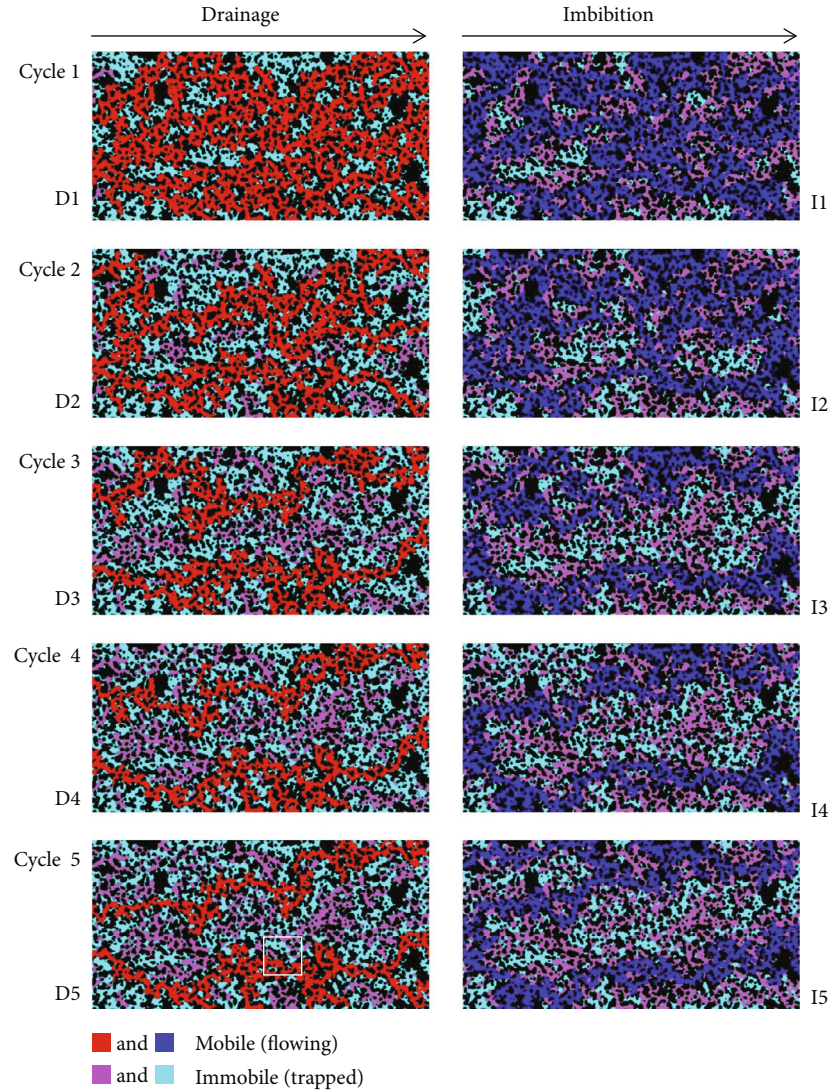


FIGURE 5: Sequential images of steady-state distribution of fluids in the micromodel after the completion of each injection cycle (mobile (flowing) hexane and water injected during drainage and imbibition cycles, respectively; immobile (trapped) hexane and water). The magnified image of the region marked with a white square in D5 is shown in Figure 8.

fluids. At the beginning of injection in each cycle, the rate of increase or decrease in hexane saturation was clearly linear with time (marked with red and blue lines in Figure 6) and can be interpreted as the displacement or injection rate of invading fluids [27, 36]. In D1, the rate of increase in hexane saturation was estimated as 1.45%/sec and can be converted to a volumetric displacement rate by multiplying the pore volume of the micromodel ($2.3 \mu\text{L}$) as $2.07 \mu\text{L}/\text{min}$, which was fairly close to the flow rate set for the injection pumps ($2.0 \mu\text{L}/\text{min}$). In this period, invading hexane progressed downstream by displacing the same volume of residing water and occupying the pore spaces. After the period of the increase in saturation, the hexane breakthrough was observed at $t = 45$ seconds, which is equivalent to 0.68 PV, and the saturation values became maximum which is defined as *displacement efficiency*. Afterward, hexane saturation remained constant, which implied that, after the breakthrough, injected hexane passed through established active

flow paths without displacing more water, and the spatial distribution of fluids in the pore network remained steady. During I1, as in the previous drainage cycle, the hexane saturation decreased at a rate proportional to the injection rate and reached the steady state after water breakthrough. In the following drainage-imbibition cycles, fairly similar patterns in hexane saturation were repeatedly followed.

Steady-state hexane saturations of drainage and imbibition cycles and their differences are shown in Figure 7. As drainage-imbibition cycles proceeded, steady-state hexane saturations in drainage cycles (S_{Di} , where i is the number of cycle), which can be defined as displacement efficiency, decreased from D1 to D2 (67.99% to 57.41%) and remained constant afterward (57.66%~59.12%). Meanwhile, those in the imbibition cycles (S_{Ii}), which can be defined as residual saturation, slightly but consistently increased over cycles (38.01% to 48.31%). Since the viscosity of hexane (0.297 cP) is significantly lower than that of water (0.890 cP), the mobility

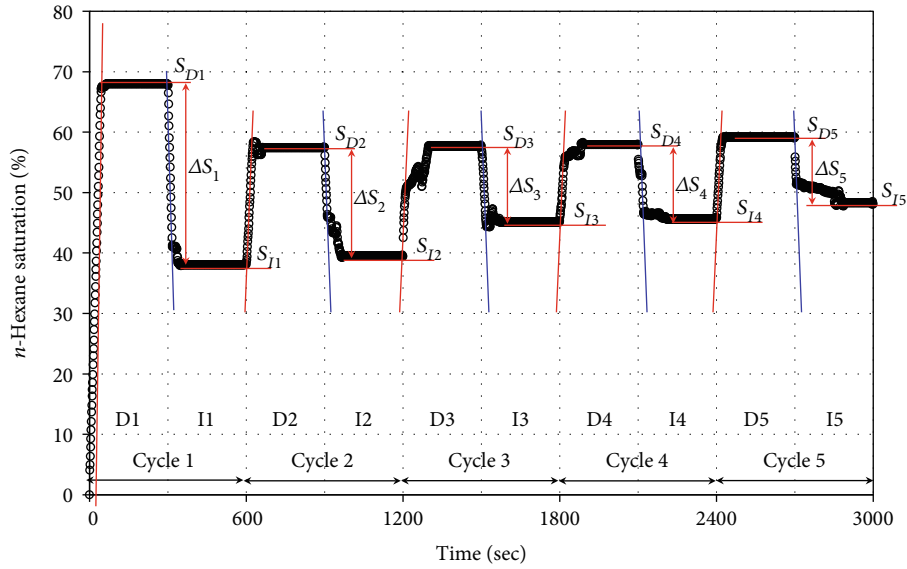


FIGURE 6: Evolution of hexane saturation throughout the five injection cycles. D: drainage, period of hexane injection; I: imbibition, period of deionized water injection. Since the micromodel is always fully saturated with hexane and deionized water, water saturation can be estimated as the complement of hexane saturation.

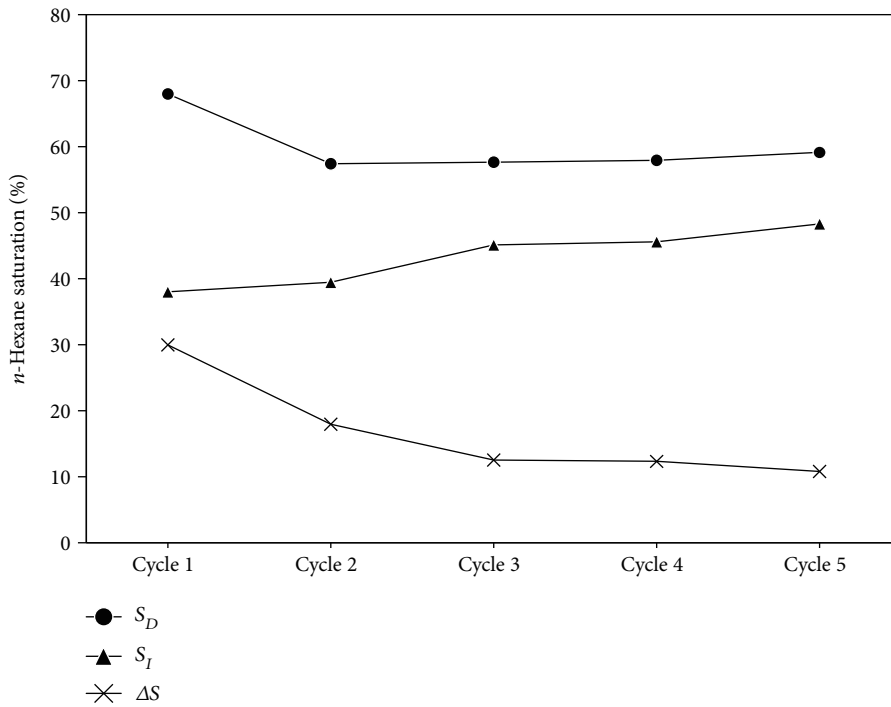


FIGURE 7: Saturation changes during cyclic injection of hexane and water.

ratio was highly favorable to displacement of hexane by injecting water and a relatively smaller amount of hexane was displaced, compared to the amount of water displaced by invading hexane in drainage cycles, after water flooding in imbibition cycles [15]. As a result, the differences between S_{D_i} and S_{I_i} (ΔS_i) decreased (29.98% to 10.81%) and converged to a constant value, as will be discussed later.

A segment of pore networks in the micromodel (marked with a white square in Figure 5) was selected,

and the flow and distribution of immiscible fluids during a cyclic injection experiment were further investigated in pore scale. Figures 8 and 9 display magnified sequential images of fluid distribution in the selected segment during drainage cycles and local steady-state saturations of hexane and water in the segment according to their mobilities. As hexane injection began into an initially water-saturated micromodel in D1, excluding dead-end pores and narrow pore throats with high capillary pressures, invading hexane

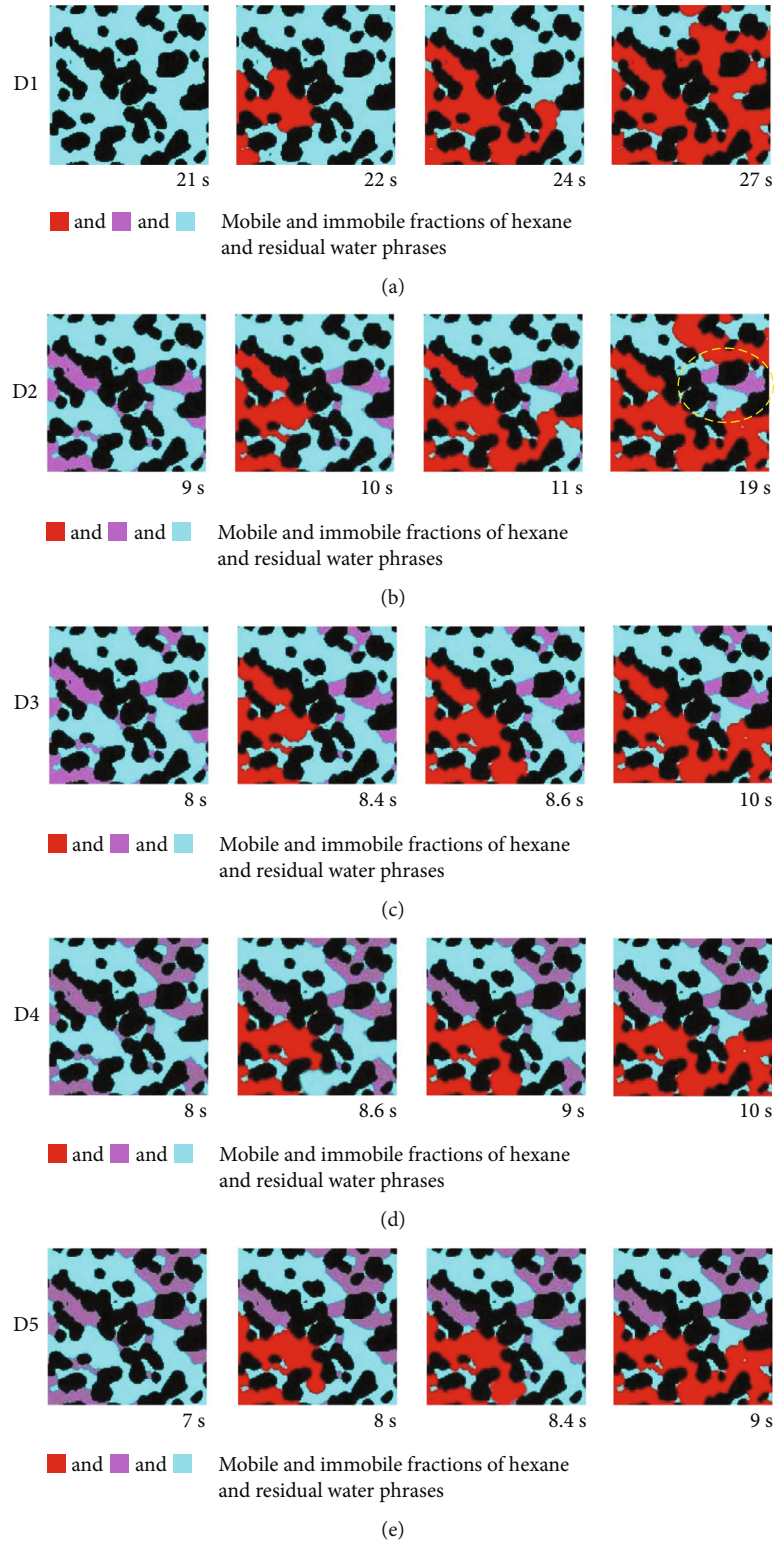


FIGURE 8: Sequential magnified images of fluid distribution in a selected segment of the micromodel during drainage cycles.

displaced most of the water residing in the segment and created flow paths (Figure 8(a)). For approximately five seconds after the appearance (22 s \rightarrow 27 s), the saturation and distribution of hexane had reached a steady state, in which the mobile fraction of hexane occupied 71.4% of pore space in the segment. Meanwhile, including two rela-

tively large pools, the residual phase of water at various sizes was observed as resulting from various residual mechanisms, such as wettability, capillarity, dead-end zone, entrapment, or bypassing [37]. After the completion of the first set of drainage-imbibition cycles, D1 and I1, hexane injection was resumed into the pore network, in

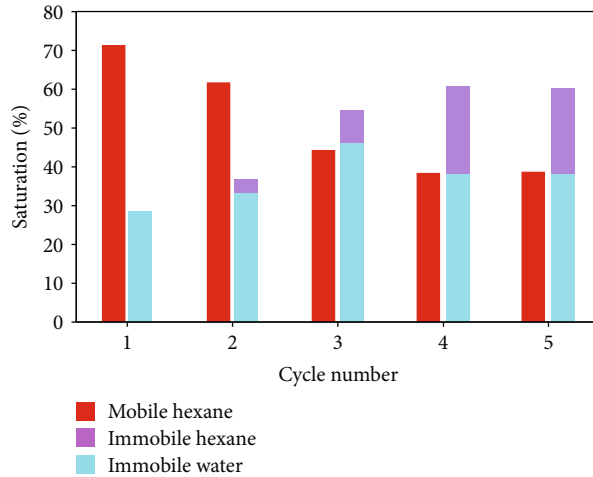


FIGURE 9: Steady-state saturations of fluids in the selected segment at drainage cycles.

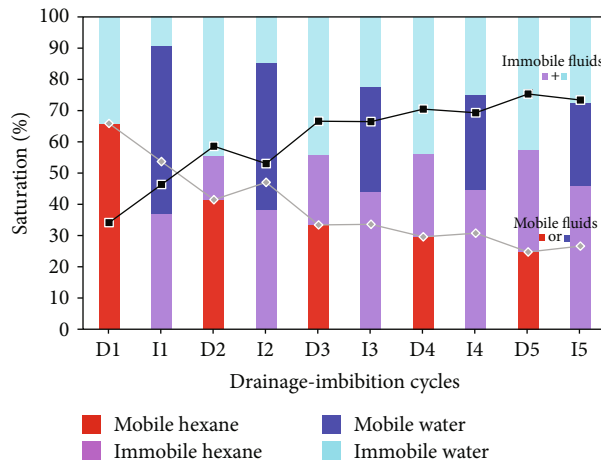


FIGURE 10: Saturation of mobile and immobile fluids over the course of five sets of drainage-imbibition cycles.

D2, in which residual phases of hexane (purple) as well as water (cyan) existed simultaneously (Figure 8(b)). Although the morphology and the pore structure of the micromodel played a major role in governing hexane flow in D1, the spatial distribution of residual hexane and water could make an additional contribution in creating flow paths for invading hexane in later drainage cycles. By building up clusters of immobile blobs with residual water, a fraction of residual hexane surrounded by residual water functioned as a blockage to obstruct the invading hexane flow (marked as a dotted yellow eclipse in Figure 8(b)). As a result, less residual water was displaced by inflowing hexane, and the final hexane saturation was reduced by 9.6%, from 71.4% at D1 to 61.8% at D2. The hysteresis effect due to discrepancy in the initial distribution of residual fluids during cyclic injection of immiscible fluids had also been observed for relative permeability of fluids inflowing to pore networks and reportedly appeared more clearly at early injection cycles [15, 38].

As cyclic injection proceeded, pore spaces filled with immobile residual hexane and water gradually grew, whereas the mobile region for invading hexane or water shrank. The saturation of immobile fluids (of both hexane and water) at drainage cycles increased from 28.6% at D1 to 55.7% at D3 and remained constant (61.5%~61.2%) in the remaining cycles. Not just saturation but also the steady-state distribution of hexane and water became almost unchanged in D4 and D5, because the immobile regions developed with entangled small-scale blobs of hexane and water that were unaffected by the invading hexane flow, which bypassed the inactive flow region. Such observations during drainage cycles were identical for invading water during the imbibition cycles. The steady-state water saturation increased from 38.0% at I1 to 45.1% at I3 and converged to 45.6%~48.3% during later cycles. Inversely proportional to the increase in saturation of immobile fluids, the pore spaces available for flow decreased as cyclic injection was repeatedly performed. Whereas the injection flow rate remained constant, the pore velocity through the mobile region increased because of the

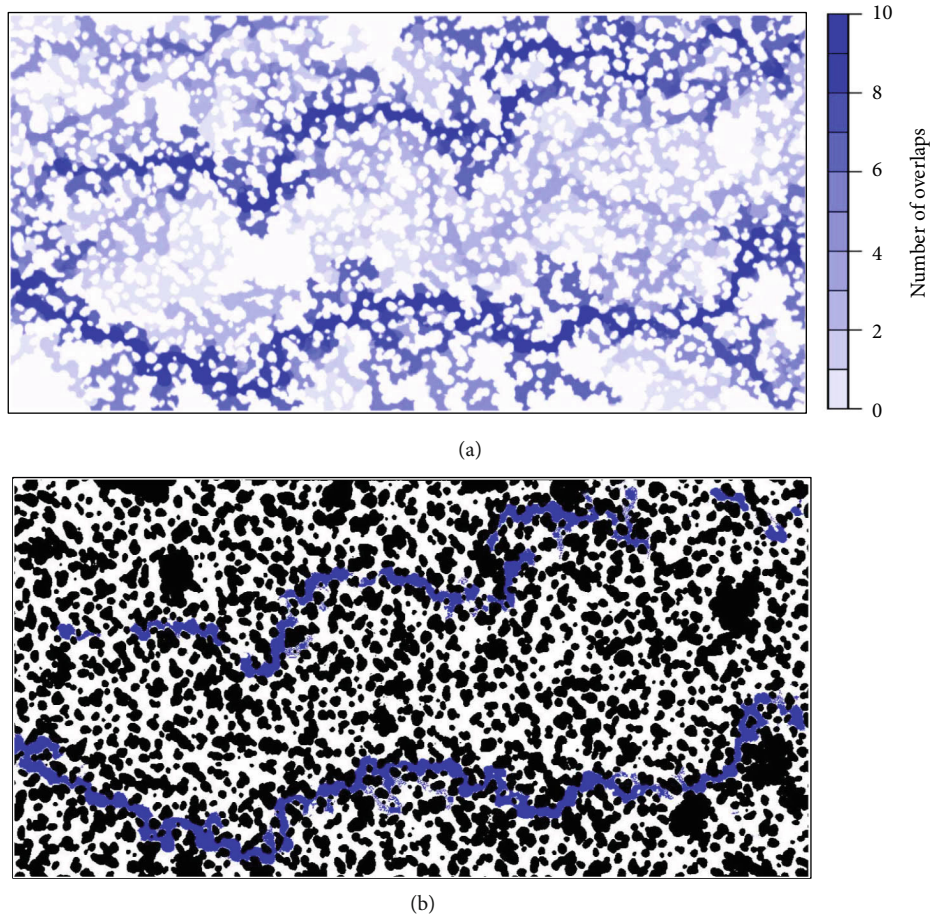


FIGURE 11: Images for flow channels in a micromodel: (a) overlapped image of flow channels formed over the course of five sets of drainage-imbibition cycles. The difference of the color indicates the number of overlapped flow channels, (b) main flow channels (number of overlaps > 9) plotted on binary image of the micromodel.

decrease in pore space available for flow and, as a result, the arrival time of hexane from the inlet to the selected segment consistently decreased, from 22 s in D1 to 8 s in D5. These results also suggested that the pore-scale observation can be reasonably upscaled to the entire micromodel.

Figure 10 shows the changes in saturations of hexane and water in the entire micromodel depending on their mobility during the cyclic injection experiment. Obviously, hexane saturation (both the mobile and immobile fractions) increased after hexane injection in the drainage cycles, whereas water saturation (mobile and immobile) increased after water injection in the imbibition cycles. Comparing them in terms of their mobility, the saturation of immobile fluids consistently increased up to around 70%, which resulted from coalescence of numerous small blobs of hexane and water trapped and entangled with each other. On the other hand, the fraction of mobile fluids representing flow paths of mobile hexane or water gradually decreased, up to around 30%, which resulted because invading fluids bypassed the immobile regions and their flow paths were getting narrower and less ramified, especially during the early injection cycles (Cycles 1–3). These observation and

quantitative analysis of the micromodel agreed with those made at pore scale. Such agreement demonstrates that the immiscible displacement at pore scale during cyclic injection has been successfully upscaled to the entire micromodel and suggests that it could further be expanded to reservoir scale.

The contribution of an individual pore space to active flow paths can be represented by the number of times the space is occupied by invading fluids during a series of cyclic injections. In order to measure the contribution, 10 multicolored images taken after the completion of each drainage or imbibition cycle were converted into binary images displaying only mobile fractions of the injected fluid. These binary images were then overlapped to identify most accessed flow paths (Figure 11(a)). Among the pixels consisting of pore spaces in a micromodel in each binary image, pixels that were overlapped more than 9 times or those that correspond to the most accessed flow paths were projected on the binary image of the micromodel (Figure 11(b)). The “main flow channels,” which were displayed as pore spaces colored in blue in the figure, considerably coincided with the flow paths observed at later drainage and imbibition cycles in Figure 6. The degree of overlaps (> 9) of the main flow channels suggested that

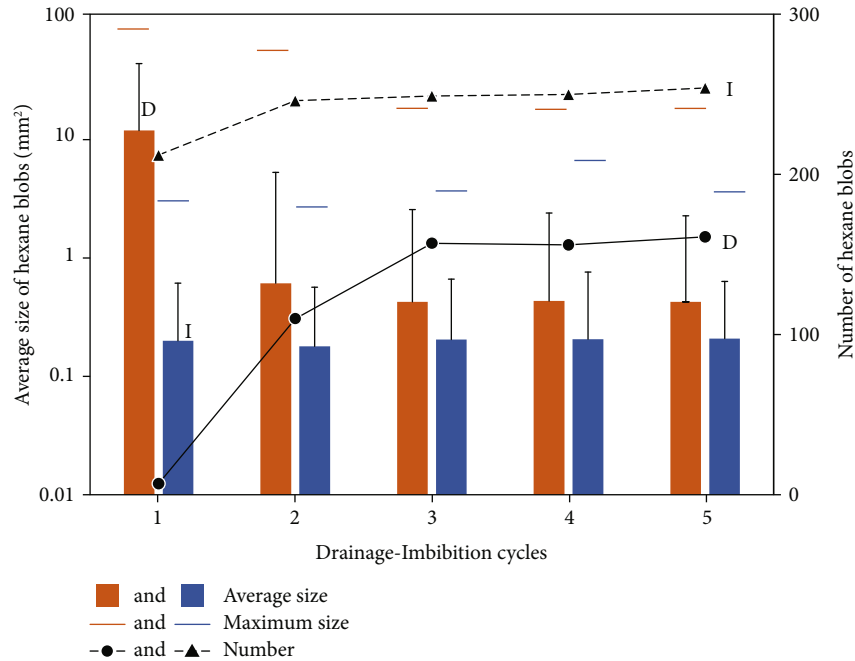


FIGURE 12: Average and maximum size and number of hexane blobs and clusters after the completion of the drainage-imbibition cycles.

they were created as core parts of mobile fractions, since the first drainage cycle started and remained functioning as flow paths regardless of the type of injecting fluids. In addition, the area of the main flow channels in the figure was measured as occupying 12.3% of the total pore space; it was similar to the differences between steady-state hexane saturation at drainage and imbibition cycles from Cycle 3 through Cycle 5 (ΔS_3 : 12.5%, ΔS_4 : 12.3%, and ΔS_5 : 10.8%) in Figure 7. That is, after the injecting fluid was shifted from hexane to water, most of the newly injected water passed through flow paths of the previously flooded hexane with minor variations. Invading hexane at later drainage cycles was also expected to follow similar flow paths. It is noteworthy that not all of the mobile fractions of injecting fluids contributed to its flow. Around 30% of the saturation of mobile fluids at later cycles, shown in Figure 10, consisted of not only active flow regions created surrounding the main flow channels but also residual blobs that merged with the main flow channels but that did not actively contribute to flow.

Multicolored images for steady-state distribution of immiscible fluids in the micromodel after the completion of drainage-imbibition cycles (Figure 5) show hexane blobs and clusters of various sizes occupying a single pore space or porous regions connecting multiple pore units [36, 39, 40]. In this study, we did quantitative analysis of hexane morphology during the cyclic injection experiments using ImageJ and in-house MATLAB codes. The number and average size of hexane blobs and clusters in the micromodel after the completion of each injection cycle are displayed in Figure 12. The average size of hexane blobs, calculated from the number of pixels representing pore spaces occupied by hexane, was largest at the first drainage cycle, in which injected hexane formed continuous streams and remained roughly constant at later drainage-imbibition cycles. It

decreased at imbibition cycles when invading water displaced hexane occupying flow paths and left small hexane blobs isolated from flow paths, but it increased at drainage cycles when invading hexane displaced water and some of the residual hexane blobs rejoined to flow paths. The maximum size of a hexane blob after drainage cycles, therefore, corresponded to the size of the largest continuous stream. However, during imbibition cycles, invading water displaced the previously flooded large-scale hexane stream and left numerous small-scale hexane blobs in the residual phase, which resulted in no significant changes in its maximum size over cycles. In contrast, the number of hexane blobs increased after both drainage and imbibition cycles, whereas that after imbibition cycles, which scattered hexane blobs, was much higher than that after drainage cycles, when scattered small-scale hexane blobs were merged with invading hexane. As a result, the average size of hexane blobs decreased but their number increased as cyclic injection proceeded, which suggested that a few large hexane blobs were separated into many small blobs [36]. The changes in the size and number of hexane blobs asymptotically decreased over multiple drainage-imbibition cycles, which indicated that the structuring of mobile regions, including main flow channels and immobile regions of residual hexane and water, was almost complete.

4. Conclusions

This study used a set of immiscible proxy fluids, *n*-hexane and deionized water, and 2D transparent micromodels to investigate the effects of cyclic injection of CO₂ and porewater into deep geological formations on the migration and residual trapping of CO₂ stored in geological carbon sequestration operations. The key results from

observations and quantitative analysis in this experimental study are as follows:

- (i) As cyclic injection of hexane and water continued, the hexane saturation repeatedly increased during drainage cycles and decreased during imbibition cycles, but the differences gradually diminished and remained constant at later cycles
- (ii) The variations in steady-state hexane saturation at drainage cycles showed a pattern of asymptotic decrease. Examining the trend in detail in terms of mobility, however, we found that the mobile fractions in hexane saturation rapidly decreased, whereas the immobile fractions consistently increased. Proportional to the increase of immobile fractions, the hexane saturation at imbibition cycles, defined as residual saturation, slightly but consistently increased over cycles
- (iii) The reduction of the mobile region or a decrease in mobile fractions of hexane saturation occurred as the randomly diverged flow paths formed at an early stage of the cycle gradually converged into less ramified ones. The pore spaces occupied by the “main flow channels” were fairly comparable to the differences in steady-state hexane saturations between later drainage and imbibition cycles, which implied that most of the newly injected fluid passed through flow paths of the previously flooded fluid with minor variations in later cycles
- (iv) The expansion of the immobile region or an increase in the immobile fractions of hexane saturation occurs as previously flooded hexane as continuous and interconnected steams was dispersed and isolated into numerous small-scale blobs by newly invading water. A conglomerate of blobs and clusters of immiscible fluids, spread in the same manner, was built up during repeated cyclic injection processes until the immobile region approached the main flow channels
- (v) The observations and analyses in this study implied that the application of cyclic injection of CO₂ and water may be used to store large-scale continuous CO₂ streams as small-scale dispersed CO₂ blobs and clusters in GCS operations. Small-scale CO₂ blobs with a high specific area can facilitate dissolution trapping into surrounding porewater and, eventually, mineral trapping [19, 41]. In addition, upward mobility of stored CO₂ can be limited because of decreased buoyancy, which is inversely proportional to volume, and increased pore pressure, which may significantly improve the effectiveness and security of geological CO₂ sequestration

Data Availability

The data used to support the findings of this study are available from the corresponding author upon request.

Conflicts of Interest

The authors declare that they have no conflicts of interest.

Acknowledgments

This research was supported by the Basic Science Research Program through the National Research Foundation of Korea (NRF) funded by the Ministry of Education (NRF-2019R111A3A01060663).

References

- [1] C. M. White, B. R. Strazisar, E. J. Granite, J. S. Hoffman, and H. W. Pennline, “Separation and capture of CO₂ from large stationary sources and sequestration in geological formations—coalbeds and deep saline aquifers,” *Journal of the Air & Waste Management Association*, vol. 53, no. 6, pp. 645–715, 2003.
- [2] IPCC, *Special Report on Carbon Dioxide Capture and Storage*, B. Metz, O. Davidson, H. Coninck, M. Loos, and L. A. Meyer, Eds., Cambridge and New York, NY, 2005.
- [3] S. Bachu, “CO₂ storage in geological media: role, means, status and barriers to deployment,” *Progress in Energy and Combustion Science*, vol. 34, no. 2, pp. 254–273, 2008.
- [4] S. Bachu, W. D. Gunter, and E. H. Perkins, “Aquifer disposal of CO₂: hydrodynamic and mineral trapping,” *Energy Conversion and Management*, vol. 35, no. 4, pp. 269–279, 1994.
- [5] W. D. Gunter, S. Bachu, and S. M. Benson, “The role of hydrogeological and geochemical trapping in sedimentary basins for secure geological storage for carbon dioxide,” in *Geological Storage of Carbon Dioxide*, S. J. Baines and R. H. Worden, Eds., pp. 129–145, Geological Society Special Publication, 2004.
- [6] S. Fobi, “Viscous effects of wetting and nonwetting fluids on capillary trapping mechanism: a climate change mitigation strategy, M.S. thesis,” Oregon State University, Corvallis, OR, 2012.
- [7] D. Wildenschild, R. T. Armstrong, A. L. Herring, I. M. Young, and J. William Carey, “Exploring capillary trapping efficiency as a function of interfacial tension, viscosity, and flow rate,” *Energy Procedia*, vol. 4, pp. 4945–4952, 2011.
- [8] S. M. Benson and D. R. Cole, “CO₂ sequestration in deep sedimentary formations,” *Elements*, vol. 4, no. 5, pp. 325–331, 2008.
- [9] A. L. Herring, E. J. Harper, L. Andersson, A. Sheppard, B. K. Bay, and D. Wildenschild, “Effect of fluid topology on residual nonwetting phase trapping: implications for geologic CO₂ sequestration,” *Advances in Water Resources*, vol. 62, pp. 47–58, 2013.
- [10] M. Soroush, D. Wessel-Berg, O. Torsaeter, and J. Kleppe, “Investigating residual trapping in CO₂ storage in saline aquifers - application of a 2D glass model, and image analysis,” *Energy Science & Engineering*, vol. 2, no. 3, pp. 149–163, 2014.
- [11] E. J. Harper, “Optimization of capillary trapping of CO₂ sequestration in saline aquifers; optimization of capillary trapping of CO₂ sequestration in saline aquifers. M.S. thesis,” Oregon State University, Corvallis, OR, 2013.
- [12] R. Juanes, E. J. Spiteri, F. M. Orr Jr., and M. J. Blunt, “Impact of relative permeability hysteresis on geological CO₂ storage,” *Water Resources Research*, vol. 42, no. 12, article W12418, 2006.

- [13] A. Kumar, M. H. Noh, R. C. Ozah et al., "Reservoir simulation of CO₂ storage in aquifers," *SPE Journal*, vol. 10, no. 3, pp. 336–348, 2005.
- [14] M. Riazi, M. Sohrabi, C. Bernstone, M. Jamiolahmady, and S. Ireland, "Visualisation of mechanisms involved in CO₂ injection and storage in hydrocarbon reservoirs and water-bearing aquifers," *Chemical Engineering Research and Design*, vol. 89, no. 9, pp. 1827–1840, 2011.
- [15] A. Saedi, R. Rezaee, B. Evans, and B. Clennell, "Multiphase flow behaviour during CO₂ geo-sequestration: emphasis on the effect of cyclic CO₂-brine flooding," *Journal of Petroleum Science and Engineering*, vol. 79, no. 3-4, pp. 65–85, 2011.
- [16] P. E. S. Bergmo, A.-A. Grimstad, and E. Lindeberg, "Simultaneous CO₂ injection and water production to optimise aquifer storage capacity," *International Journal of Greenhouse Gas Control*, vol. 5, no. 3, pp. 555–564, 2011.
- [17] H. Shamshiri and B. Jafarpour, "Controlled CO₂ injection into heterogeneous geologic formations for improved solubility and residual trapping," *Water Resources Research*, vol. 48, no. 2, article W02530, 2012.
- [18] E. H. Kimbrel, A. L. Herring, R. T. Armstrong, I. Lunati, B. K. Bay, and D. Wildenschild, "Experimental characterization of nonwetting phase trapping and implications for geologic CO₂ sequestration," *International Journal of Greenhouse Gas Control*, vol. 42, pp. 1–15, 2015.
- [19] A. L. Herring, L. Andersson, and D. Wildenschild, "Enhancing residual trapping of supercritical CO₂ via cyclic injections," *Geophysical Research Letters*, vol. 43, no. 18, pp. 9677–9685, 2016.
- [20] F. A. Malekzadeh, Y. Leonenko, and M. Dusseault, "Cyclic injection of CO₂ into a saline aquifer with extended interface," *International Journal of Global Environmental Issues*, vol. 16, no. 4, p. 231, 2017.
- [21] A. González-Nicolás, L. Trevisan, T. H. Illangasekare, A. Cihan, and J. T. Birkholzer, "Enhancing capillary trapping effectiveness through proper time scheduling of injection of supercritical CO₂ in heterogeneous formations," *Greenhouse Gases: Science and Technology*, vol. 7, no. 2, pp. 339–352, 2017.
- [22] K. Edlmann, S. Hinchliffe, N. Heinemann, G. Johnson, J. Ennis-King, and C. I. McDermott, "Cyclic CO₂ - H₂O injection and residual trapping: implications for CO₂ injection efficiency and storage security," *International Journal of Greenhouse Gas Control*, vol. 80, pp. 1–9, 2019.
- [23] Z. Zhang and R. Agarwal, "Numerical simulation and optimization of CO₂ sequestration in saline aquifers for enhanced storage capacity and secured sequestration," *International Journal of Energy and Environment*, vol. 4, pp. 387–398, 2013.
- [24] A. Abedini and F. Torabi, "Parametric study of the cyclic CO₂ injection process in light oil systems," *Industrial & Engineering Chemistry Research*, vol. 52, no. 43, pp. 15211–15223, 2013.
- [25] J. Ma, X. Wang, R. Gao et al., "Study of cyclic CO₂ injection for low-pressure light oil recovery under reservoir conditions," *Fuel*, vol. 174, pp. 296–306, 2016.
- [26] B. Wei, L. Lu, W. Pu et al., "Production dynamics of CO₂ cyclic injection and CO₂ sequestration in tight porous media of Lucaogou formation in Jimsar sag," *Journal of Petroleum Science and Engineering*, vol. 157, pp. 1084–1094, 2017.
- [27] A. R. Adebayo, "Viability of foam to enhance capillary trapping of CO₂ in saline aquifers—an experimental investigation," *International Journal of Greenhouse Gas Control*, vol. 78, pp. 117–124, 2018.
- [28] Y. Assef, A. Kantzas, and P. Pereira Almaso, "Numerical modelling of cyclic CO₂ injection in unconventional tight oil resources; trivial effects of heterogeneity and hysteresis in Bakken formation," *Fuel*, vol. 236, pp. 1512–1528, 2019.
- [29] U. Griggull and E. Schmidt, *Properties of Water and Steam in SI-Unit. Second Revised and Updated Printing*, Springer-Verlag, 1979.
- [30] S. Bachu and D. Brant Bennion, "Dependence of CO₂ -brine interfacial tension on aquifer pressure, temperature and water salinity," *Energy Procedia*, vol. 1, no. 1, pp. 3157–3164, 2009.
- [31] L. Trevisan, A. Cihan, F. Fagerlund et al., "Investigation of mechanisms of supercritical CO₂ trapping in deep saline reservoirs using surrogate fluids at ambient laboratory conditions," *International Journal of Greenhouse Gas Control*, vol. 29, pp. 35–49, 2014.
- [32] R. Lenormand, E. Touboul, and C. Zarcone, "Numerical models and experiments on immiscible displacements in porous media," *Journal of Fluid Mechanics*, vol. 189, pp. 165–187, 1988.
- [33] S. Zeppieri, J. Rodríguez, and A. L. López de Ramos, "Interfacial tension of alkane + water systems," *Journal of Chemical & Engineering Data*, vol. 46, no. 5, pp. 1086–1088, 2001.
- [34] IAPWS (The International Association for the Properties of Water and Steam), *Release on the IAPWS Formulation 2008 for the Thermodynamic Properties of Seawater*, Berlin, Germany, 2008.
- [35] Y. Wang, C. Zhang, N. Wei et al., "Experimental study of crossover from capillary to viscous fingering for supercritical CO₂-water displacement in a homogeneous pore network," *Environmental Science & Technology*, vol. 47, no. 1, pp. 212–218, 2013.
- [36] R. Hu, J. Wan, Y. Kim, and T. K. Tokunaga, "Wettability effects on supercritical CO₂-brine immiscible displacement during drainage: pore-scale observation and 3D simulation," *International Journal of Greenhouse Gas Control*, vol. 60, pp. 129–139, 2017.
- [37] H. Ahn, S.-O. Kim, M. Lee, and S. Wang, "Effect of cyclic injection on migration and trapping of immiscible fluids in porous media," *Economic and Environmental Geology*, vol. 52, p. 12, 2019.
- [38] D. B. Bennion, F. B. Thomas, A. K. M. Jamaluddin, and T. Ma, "The effect of trapped critical fluid saturations on reservoir permeability and conformance," in *Proceedings of Annual Technical Meeting of the Petroleum Society of CIM*, Calgary, Canada, 1998.
- [39] H. Geistlinger, I. Ataei-Dadavi, S. Mohammadian, and H.-J. Vogel, "The impact of pore structure and surface roughness on capillary trapping for 2-D and 3-D porous media: comparison with percolation theory," *Water Resources Research*, vol. 51, no. 11, pp. 9094–9111, 2015.
- [40] L. Wang, S. Yang, X. Peng et al., "An improved visual investigation on gas-water flow characteristics and trapped gas formation mechanism of fracture-cavity carbonate gas reservoir," *Journal of Natural Gas Science and Engineering*, vol. 49, pp. 213–226, 2018.
- [41] A. L. Herring, L. Andersson, S. Schlüter, A. Sheppard, and D. Wildenschild, "Efficiently engineering pore-scale processes: the role of force dominance and topology during nonwetting phase trapping in porous media," *Advances in Water Resources*, vol. 79, pp. 91–102, 2015.